MATERIALS SCIENCE

Achieving room-temperature brittle-to-ductile transition in ultrafine layered Fe-Al alloys

Lu-Lu Li[1], Yanqing Su[2], Irene J. Beyerlein[2,3]*, Wei-Zhong Han[1]*

Fe-Al compounds are of interest due to their combination of light weight, high strength, and wear and corrosion resistance, but new forms that are also ductile are needed for their widespread use. The challenge in developing Fe-Al compositions that are both lightweight and ductile lies in the intrinsic tradeoff between Al concentration and brittle-to-ductile transition temperature. Here, we show that a room-temperature, ductile-like response can be attained in a FeAl/$FeAl_2$ layered composite. Transmission electron microscopy, nanomechanical testing, and ab initio calculations find a critical layer thickness on the order of 1 μm, below which the $FeAl_2$ layer homogeneously codeforms with the FeAl layer. The $FeAl_2$ layer undergoes a fundamental change from multimodal, contained slip to unimodal slip that is aligned and fully transmitting across the FeAl/$FeAl_2$ interface. Lightweight Fe-Al alloys with room-temperature, ductile-like responses can inspire new applications in reactor systems and other structural applications for extreme environments.

INTRODUCTION

A number of material structural applications in need of lightweight materials, which can withstand large deformations without cracking, are growing rapidly as energy and fuel efficiency become paramount. Fe-Al alloys have the perfect combination of light weight, high strength, wear resistance, and corrosion resistance (*1*–*3*), making them a leading candidate for bulk structures and protective coatings for service in extreme environments (*4*, *5*). For instance, there is interest in using Fe-Al alloys as an effective transition layer to reduce the thermal mismatch between the stainless steel substrate and Al_2O_3 coating in tritium storage (*6*). However, the lighter weight (Al-rich) compositions of Fe-Al alloys are disappointingly brittle at room temperature and susceptible to premature failure (*7*–*9*).

The roadblock in using Fe-Al alloys lies in the intrinsic tradeoff between increasing Al concentrations and increasing the brittle-to-ductile transition (BDT) temperature. For the heavier, Fe-Al alloys located in the Al-poor part [far less than 50 atomic % (at %) Al) of the binary Fe-Al phase diagram, the BDT temperature lies around 200°C (*10*). As the Al concentration increases further, the BDT temperature increases (*11*), until an Al concentration of 40 at %, when it jumps sharply, reaches to 800°C (*12*, *13*), a temperature far exceeding that which could be practically used in service.

The Al-rich Fe-Al phases, like $FeAl_2$, Fe_2Al_5, and $FeAl_3$ (*14*), are intermetallics that are intrinsically brittle at room temperature (*15*) and hence partly responsible for the embrittlement of Al-rich Fe-Al alloys. Hardness and mechanical testing find that their individual fracture toughness values are similar to those of ceramics and glasses (*9*). These phases have a low-symmetry crystal structure, rendering them highly anisotropic and lacking a sufficient number of preferred, easy slip modes to plastically respond uniformly in all crystallographic directions. Exact data on the individual BDT temperatures of $FeAl_2$, Fe_2Al_5, and $FeAl_3$ are currently lacking, but generally, it lies above 800°C. Unlike the intermetallic Al-rich, Fe-Al phases, the Al-poor phase, FeAl, exhibits relatively ductile failure. It has a B2-ordered structure, and its primary slip mode is (110)⟨111⟩ (*13*), which is similar to the preferred slip mode in ductile body-centered cubic (BCC) metals, like Fe.

One approach to improving the mechanical properties of Fe-Al alloys is to "complicate" their internal microstructure by introducing a high density of biphase interfaces (*16*–*21*). Deformation response is highly sensitive to the modes of dislocation slip activated within the crystals when strained. Several studies have shown that biphase interfaces in nanolaminated metals can act as sources or sinks for dislocations and through specific interactions with other dislocations and defects, like twins and vacancies, radically improve material mechanical and radiation properties (*22*–*30*). Nanolayering, wherein the spacing between adjacent biphase interfaces are on the order of 1 μm or less, has led to 5- to 10-fold increases in room-temperature strength, especially when the spacing decreases to the nanoscale (<200 nm) (*16*–*30*). However, these boosts in strength are often accompanied by decreases in ductility, toughness, or strains to failure. Nanolayered, two-phase FeAl/$FeAl_2$ composites have been studied at elevated temperatures, but in this case, the $FeAl_2$ phase creeps (*31*). To form a nanolayered Fe-Al system with an even higher density of biphase interfaces, stacks of multiple Fe/FeAl alloy foils were sintered (*32*). While high, room-temperature strength was achieved, the Fe/FeAl interfaces between the foils eventually delaminated under further deformation (*32*).

In this study, we fabricate a lightweight, eutectoid Fe-Al alloy with alternating FeAl/$FeAl_2$ layers with individual layer thicknesses ranging from 2.5 μm to 259 nm. We show that room-temperature, ductile-like behavior can be attained at the submicron layer thicknesses. Below a critical bilayer thickness of 1 μm, the mechanical response of the $FeAl_2$ phase drastically alters from typical localized, unstable cracking to homogeneous and stable flow. With a combination of nanomechanical testing, transmission electron microscopy (TEM), and ab initio calculations, we show that the transformation can be tied to fundamental change in slip pattern of the $FeAl_2$ phase from multimodal, fully contained slip to unimodal slip that is aligned and transmitting across the FeAl/$FeAl_2$ interface. The conducted slip system that the nanophase $FeAl_2$ adopts is identified as

[1]Center for Advancing Materials Performance from the Nanoscale, State Key Laboratory for Mechanical Behavior of Materials, Xi'an Jiaotong University, Xi'an 710049, China. [2]Department of Mechanical Engineering, University of California, Santa Barbara, CA 93106-5070, USA. [3]Materials Department, University of California, Santa Barbara, CA 93106-5070, USA.
*Corresponding author. Email: wzhanxjtu@mail.xjtu.edu.cn (W.-Z.H.); beyerlein@ucsb.edu (I.J.B.)

an unusually hard system and not the same as those activated in coarser $FeAl_2$. This finding suggests there are many interesting and fundamental aspects in interface-dominant intermetallic/metallic interfaces to explore. From a technological viewpoint, an Al-rich, lightweight FeAl with room-temperature, ductile-like response opens up new applications for these alloys as loading bearing structures in extreme environments.

RESULTS

Layer structures and indentation

We made eutectoid FeAl/$FeAl_2$ layered material with five different bilayer thicknesses, t = 2.5 μm, 2 μm, 1.5 μm, 1 μm, 500 nm, and 259 nm. Figure 1 shows the phase diagram of Fe-Al alloy and the morphology of a partially lamellar and a fully lamellar region for the case in which the bilayer thickness t is 1 μm. The microstructure consists of regularly alternating FeAl and $FeAl_2$ layers. The FeAl phase has a B2 structure, while the $FeAl_2$ phase has a triclinic structure (Fig. 1D) (*33*–*35*). Figure 1E provides a closer view of the layered FeAl/$FeAl_2$ region as a bright-field TEM image. The FeAl/$FeAl_2$ interfaces are planar at this nanometer scale and some pre-existing dislocations can be seen lying within the relatively thicker $FeAl_2$ layers. We used TEM to identify the orientation relationship of the interface in the FeAl/$FeAl_2$ layered material (Fig. 1F). As labeled in Fig. 1F, the FeAl/$FeAl_2$ interface has an interface plane of $(11\bar{3})_{FeAl_2}//(101)_{FeAl}$. The interface plane corresponds to a slip plane in the FeAl phase, suggesting that the interface could be prone to interfacial sliding.

We perform Micro Vickers indentation tests at room temperature using relatively high loads to impose sufficiently large strains on layered FeAl/$FeAl_2$ material of all thicknesses t to determine whether the failure behavior would be ductile like or brittle like. Figure 2 compares their indentation response with that of single-phase (nonlayered) $FeAl_2$. Despite sharing the same eutectoid composition, the responses of the layered materials change from brittle to ductile like as t reduces below 1 μm. Crack formation in the thicker layered sample (t > 2 μm) results from the limited amount of mobile dislocations in carrying plasticity needed to accommodate the applied strain (*27*–*30*). The finest layer of 259 nm exhibits a fully ductile-like response at room temperature. Several repeated tests on the 259-nm eutectoid FeAl/$FeAl_2$ material find the same ductile-like response. This same material also achieves the highest hardness. As indicated in Fig. 2, as t decreases, the hardness of the layered eutectoid FeAl/$FeAl_2$ at first deceases, but then increases. On the basis of these initial tests, this finest material is already showing signatures of simultaneous high strength and toughness.

To understand how the BDT happened, basic deformation properties of the individual phases, FeAl and $FeAl_2$, are studied first. Nanoindentation, which imposes light compressive loads and creates only 1-μm imprints, is made in areas that are either fully FeAl or $FeAl_2$ (fig. S1A). With relatively small loads and shallow indentation depths, the FeAl and $FeAl_2$ phases do not show a notable difference in deformation response (fig. S1B). From these nanoindentation tests, the hardness and Young's modulus values are extracted. As shown in fig. S1C, these properties are nearly the same for these two

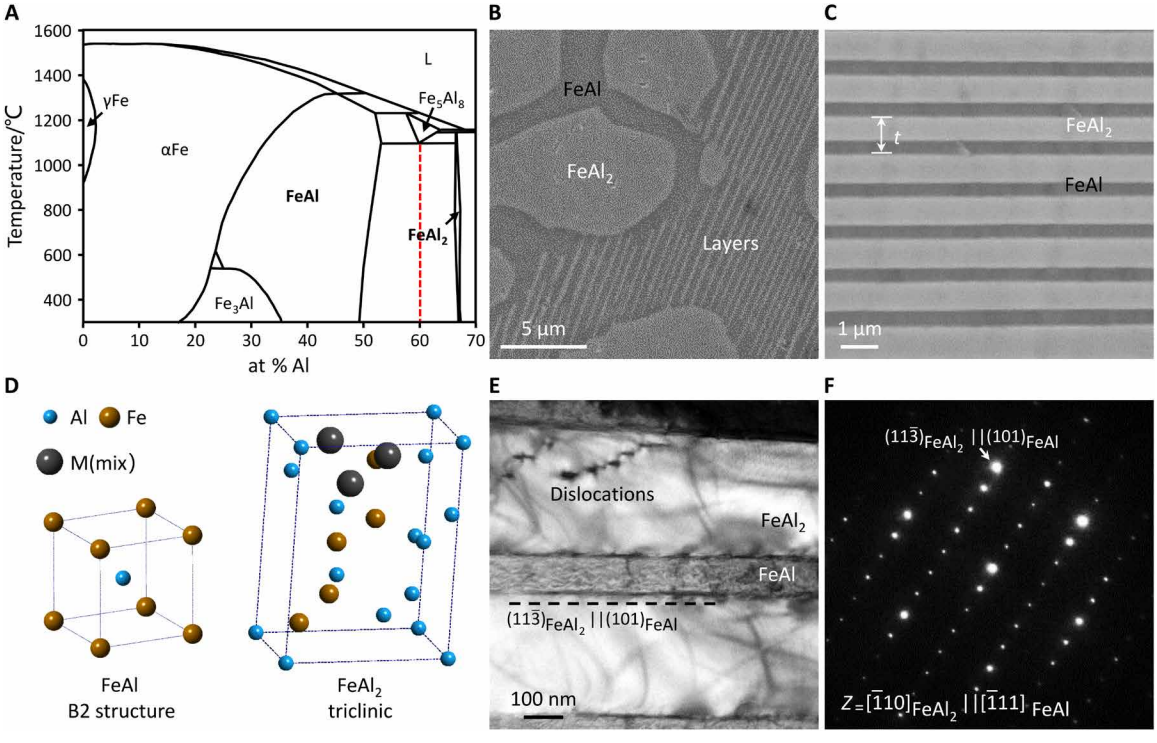

Fig. 1. The morphology and structure of FeAl and $FeAl_2$. (**A**) Binary Fe-Al phase diagram (*10*, *14*). The red dotted line indicates the alloy composition in this work. (**B**) Typical scanning electron microscope (SEM) micrographs of the FeAl alloy with both FeAl and $FeAl_2$ phases. (**C**) Typical SEM image of the FeAl alloy with a layered morphology in which the bright phase is $FeAl_2$ and the dark phase is FeAl. The thickness is defined as the total thickness of one layer of FeAl and one layer of $FeAl_2$ (as marked in the figure). (**D**) Crystal structures of FeAl and $FeAl_2$. (**E**) Typical TEM micrographs of the layered FeAl/$FeAl_2$ alloy. (**F**) The selected-area electron diffraction pattern of the layered FeAl/$FeAl_2$ alloy showing that it has an interface orientation relationship of $[\bar{1}10]_{FeAl_2}//[\bar{1}11]_{FeAl}$ and $(11\bar{3})_{FeAl_2}//(101)_{FeAl}$.

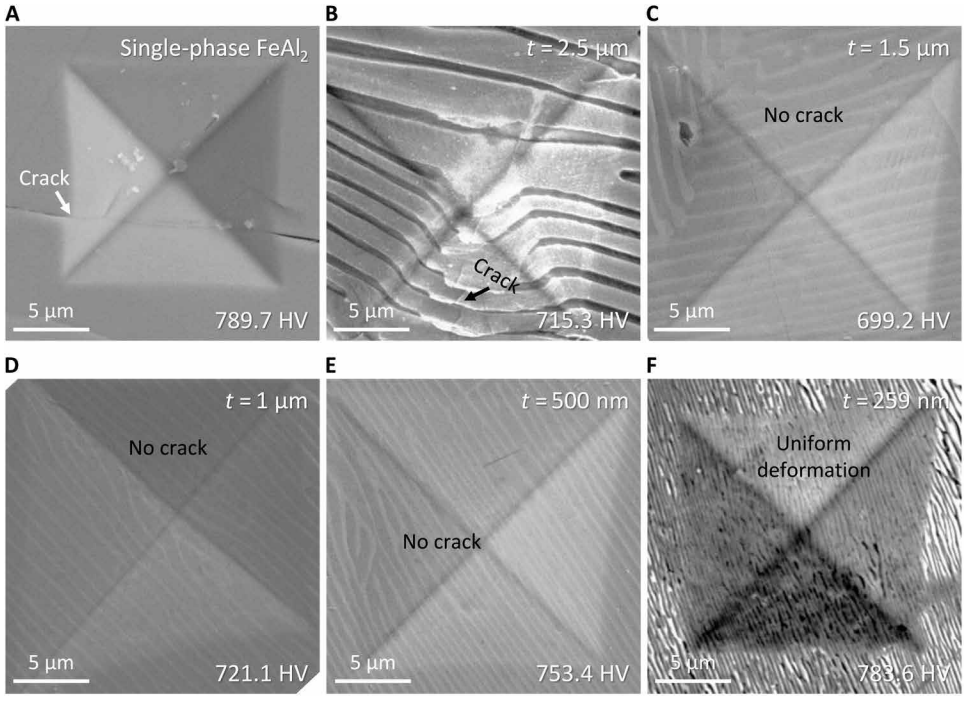

Fig. 2. Comparison of indentations. (**A**) Typical SEM micrographs of the indentation site in single-phase $FeAl_2$. (**B** to **F**) Typical SEM micrographs of the indentations in the layered FeAl/$FeAl_2$ with an average phase thicknesses of 2.5 μm, 1.5 μm, 1 μm, 500 nm, and 259 nm. The hardness is also labeled in the figure. HV is the unit for the Vickers hardness.

phases, with the $FeAl_2$ phase showing a slightly higher hardness than the FeAl phase. The Young's modulus of these two phases is both close to 200 GPa. These tests were repeated at the FeAl/$FeAl_2$ interface, wherein the nanoindentation imprint spans both materials. The Young's modulus of the interface region was similar to that of its adjoining materials, and the hardness of interface lies in between the hardness of these two phases.

Deformation structures in single-phase FeAl and $FeAl_2$

Next, we studied the indentation deformation response of the FeAl material alone, which is expected to be ductile. As mentioned, the FeAl phase has a B2 crystal structure and 12 $\{110\}\langle 111\rangle$ slip systems available for plastic deformation similar to metals with a BCC crystal structure. We cut thin foils for TEM analysis from the Micro Vickers indentation tests using a focused ion beam (FIB) lifting technique, as illustrated in fig. S2A, to determine the slip patterns resulting from the deformation. From the bright- and dark-field TEM images in fig. S2B, we find that the B2 FeAl phase exhibits undeniable signs of ductile-like behavior. The deformation microstructures after indention are homogeneous, with no localized slip bands and no cracks.

Using the same procedure, the response of single-phase $FeAl_2$ is examined. Plastic straining in this Al-rich alloy is known to be limited and its failure is brittle like. Figure S3 (A and B) shows the scanning electron microscope (SEM) analyses of the indentation deformation in single-phase $FeAl_2$. A crack has propagated across the indentation with a shear offset of 629 nm. In another region, cracks have not only formed but many shear faults are also produced at the edge of the indentation (fig. S3B). The deformation of single-phase $FeAl_2$ is brittle, unlike the FeAl phase and the ultrafine layered composite seen in Fig. 2.

Under the SEM imaging conditions in fig. S2C, there are no signs of shear deformation accompanying the fracture of the $FeAl_2$ phase. To identify any microscopic plastic deformation mechanisms that may have preceded cracking and occurred at a finer scale than can be accessed via SEM, we performed TEM analysis in areas both distant from the crack, where plasticity may have developed, and immediately surrounding the crack. Figure S2 (D to F) shows TEM images of those regions marked D and E, far to the left of the crack. The TEM analysis exposes evidence of heterogeneous plastic deformation in the form of highly localized slip bands on specific crystallographic slip planes $(1\bar{5}3)$, $(\bar{1}13)$, $(0\bar{4}6)$, and $(2\bar{6}0)$. The slip direction within these planes cannot be determined. In region E in fig. S2C, plastic strain is localized specifically on the $(0\bar{4}6)$ and the $(2\bar{6}0)$ planes, as marked in fig. S2E. In region F at the crack, close inspection reveals several tiny shear offsets on the left side of the crack, which have been produced by the slip bands along the $(\bar{1}13)$ plane.

The foregoing analysis establishes that at room temperature, the FeAl phase and $FeAl_2$ phase are markedly distinct in their indention failure behavior, with the FeAl phase being plastically soft with desirable homogeneous, uniform deformation and the $FeAl_2$ phase being plastically limited, localizing strain rapidly and nonuniformly and ultimately cracking.

Deformation structures in layered FeAl/$FeAl_2$

Using both SEM and TEM to analyze the deformation processes under the indenters, such as those shown in Fig. 2, we proceed to study the failure behavior of the eutectoid lamellar FeAl/$FeAl_2$ material. As seen in Fig. 2B, indentation testing of the coarsest layered FeAl/$FeAl_2$ material made (with $t = 2.5$ μm) results in cracking. While cracking is not as extensive as in the single-phase $FeAl_2$ sample, its failure can still be considered brittle like. As marked in fig. S3C, the loading has induced a relatively small crack across the $FeAl_2$ layer. Unlike the single-phase $FeAl_2$, the crack is, however, fully contained

in the $FeAl_2$ layer, and it is obstructed from propagating further by the adjacent ductile FeAl layers. The cracking occurs in favor of plasticity because of the difficulty in activating dislocation sources and moving dislocations within $FeAl_2$ (*27*–*30*). The ductile FeAl phase has experienced straining under indentation, while no such deformation other than cracking is evident in $FeAl_2$. This eutectoid composite exhibits a failure response that is, therefore, a composite of the individual responses of its constituents, wherein each phase acts the same as if it were deforming alone. The imposed strains are accommodated mostly by the ductile FeAl phase.

As seen in Fig. 2 (C to F), for the eutectoid FeAl/$FeAl_2$ alloys with an average bilayer thickness of 2 μm and below, indentation loads were not accommodated by cracking. Figure 3 shows the indentation deformation behavior of the t = 2 μm layered material. After indentation, both the FeAl and $FeAl_2$ layers deform plastically with no cracking, as shown in Fig. 3A. Figure 3 (B to F) displays the deformation microstructures that typically form underneath the indentation. Several widely spaced, crystallographically distinct slip bands developed in the $FeAl_2$ layers, along the (312), (1$\bar{2}$3), (213), (114), and (221) planes, as marked in Fig. 3. The slip planes of these bands are different from those seen in single-phase $FeAl_2$. The density of slip bands in the $FeAl_2$ phase is high and plastic flow is inhomogeneous relative to the FeAl phase, which has developed no bands. The adjoining ductile FeAl layers have blunted and stopped these $FeAl_2$ slip bands from propagating a similar slip band across it. Semicircular dark strain contrasts arise in the FeAl layer, as marked by black arrows in Fig. 3E, as a result of the stress concentrations, where the slip bands in $FeAl_2$ meet the FeAl/$FeAl_2$ interface. The FeAl phase with its many available easy slip systems within the {110}⟨111⟩ slip mode has diffused these stress concentrations. Unlike the $FeAl_2$ phase, dense delocalized dislocation structures can be seen inside the FeAl layers, in Fig. 3 (B and E), a sign of homogeneous deformation. Evidently, as the layer thickness decreases, the higher interface/volume ratio increases, leading to statistically more interfacial sites for dislocation nucleation (*27*–*30*). With more plasticity from mobile dislocations acting on more slip planes, the intensities of stress concentrations in $FeAl_2$ are softened, reducing the driving forces for $FeAl_2$ cracking.

In some regions, the deformation behavior of FeAl and $FeAl_2$ was not so dissimilar. Figure 3F highlights a likely slip transmission event from the $FeAl_2$ to the FeAl layers, as marked by the white arrows. The slip localization starts in the $FeAl_2$ layer, stops at the FeAl/$FeAl_2$ interface, and triggers slip in the FeAl layers, as marked in Fig. 3F. Once the shear from $FeAl_2$ transfers through the interface, the localized strain is dispersed by the ductile FeAl layer, and only a few diffused slip lines remain, as labeled in Fig. 3F. The scattering of localized strain in the $FeAl_2$ phase by slip transmission across the FeAl/$FeAl_2$ interface appears to be the key to thwarting strain localization in layered Fe-Al alloy. However, this behavior is not dominant across the material.

When reducing the layer thickness from t = 2 μm to t = 1.5 μm in the layered FeAl/$FeAl_2$ alloy, plastic deformation in the $FeAl_2$ layers occurs by comparatively more distributed slip, wherein the slip bands are less intense and more closely spaced, as shown in Fig. 4A. Yet still, as in the t = 2 μm layered material, these bands develop on several crystallographically distinct planes. Figure 4 (A to C) displays the deformation microstructures with these bands marked underneath the indentation. We characterized these slip band crystallographic planes as (1$\bar{1}$1), (20$\bar{1}$), (012), and (213), which are notably different from those observed in the t = 2 μm and t = 2.5 μm layered materials. The adjoining FeAl layers have blocked and dispersed the localized strain from these bands in $FeAl_2$ layers, as shown by the strain contrasts at the interface in Fig. 4 (A and C). Even in some regions, the shear strain has localized along some preferential

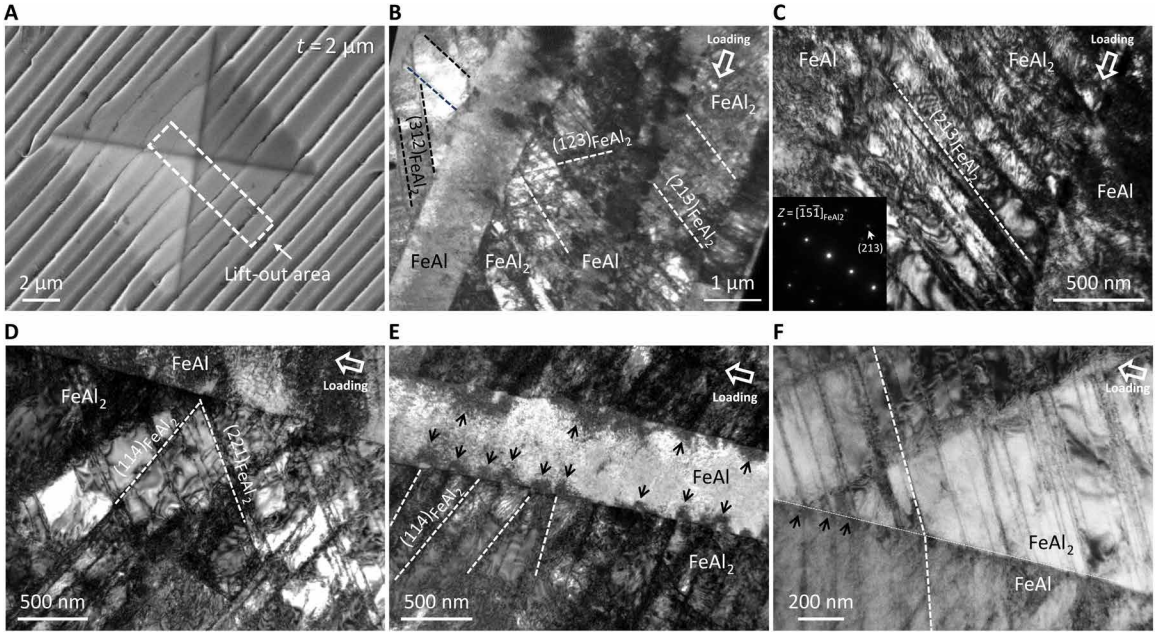

Fig. 3. Deformation of layered FeAl/$FeAl_2$ (t = 2 μm). (**A**) SEM micrographs of an indentation on layered FeAl/$FeAl_2$ with an average thickness of 2 μm. (**B** to **D**) Typical TEM micrographs showing the character of the slip bands in the $FeAl_2$ phase. (**E**) Stress concentration induced–contrast at the interface in the FeAl layer. (**F**) Slip transmission pathway across the FeAl/$FeAl_2$ interface.

crystallographic planes. TEM analysis of the interface in Fig. 4B indicates that the FeAl phase layers have accommodated the localized strain generated by the $FeAl_2$ slip bands, by permitting short slip steps to protrude at the interface into the FeAl. Here, crack nucleation has been avoided.

Codeformation in ultrafine layered FeAl/$FeAl_2$

As shown in Fig. 2 (C to D), the indentation surfaces for the layered Fe-Al alloy with an average layer thickness below 1 μm are smooth and bear no cracks. Figure 4D shows a low magnification of the deformed layer structures underneath the indentation of the 500-nm case. Signatures of codeformation between the FeAl and $FeAl_2$ layers become prominent. Codeformation means that both layers are accommodating deformation similarly and homogeneously. While the layers near the center of the indentation imprint are bent, the interfaces within this deformed region still maintain their original orientation relationship, and slip bands still cannot cut across the FeAl/$FeAl_2$ layers so easily. TEM analyses in Fig. 4 (E and F) provide more details on the substructures produced within the FeAl and $FeAl_2$ layers. Two major slip band variants have formed within the $FeAl_2$ layers. These two types of slip bands interact an angle of 75°, forming a crisscross configuration, as marked in Fig. 4F. This duplex slip pattern is well recognized for accommodating multidirectional straining and avoiding cracking (*36*). These slip bands are found to occur on the (101), (12$\bar{3}$), and (2$\bar{1}$4) slip planes. The (101)[111] slip system, which is similar crystallographically to the preferred slip mode in the FeAl phase, appears prominent in the $FeAl_2$ phase at this finer layer thickness and was not observed at the larger layer thicknesses. The spacing and intensity of these slip bands in the t = 500 nm sample are much smaller and weaker, respectively, than those in samples with larger layer thicknesses t = 2 and 1.5 μm (Figs. 3 and 4, A to C), indicating more homogeneous plasticity. We observe a series of tiny shear steps form along the interface, as marked by the black arrows in Fig. 4E. In some locations, the slip bands almost penetrate the ductile FeAl layers, as marked in Fig. 4E, but nonetheless, no cracks are produced from these protrusions.

The Fe-Al alloy with the finest average layer thickness of t = 259 nm exhibits room-temperature, ductile-like behavior. Unlike the thicker layered samples, prevalent homogenous plastic deformation occurs in both phases for this material. Signatures of homogeneous deformation manifest by the formation of a high density of weak slip bands

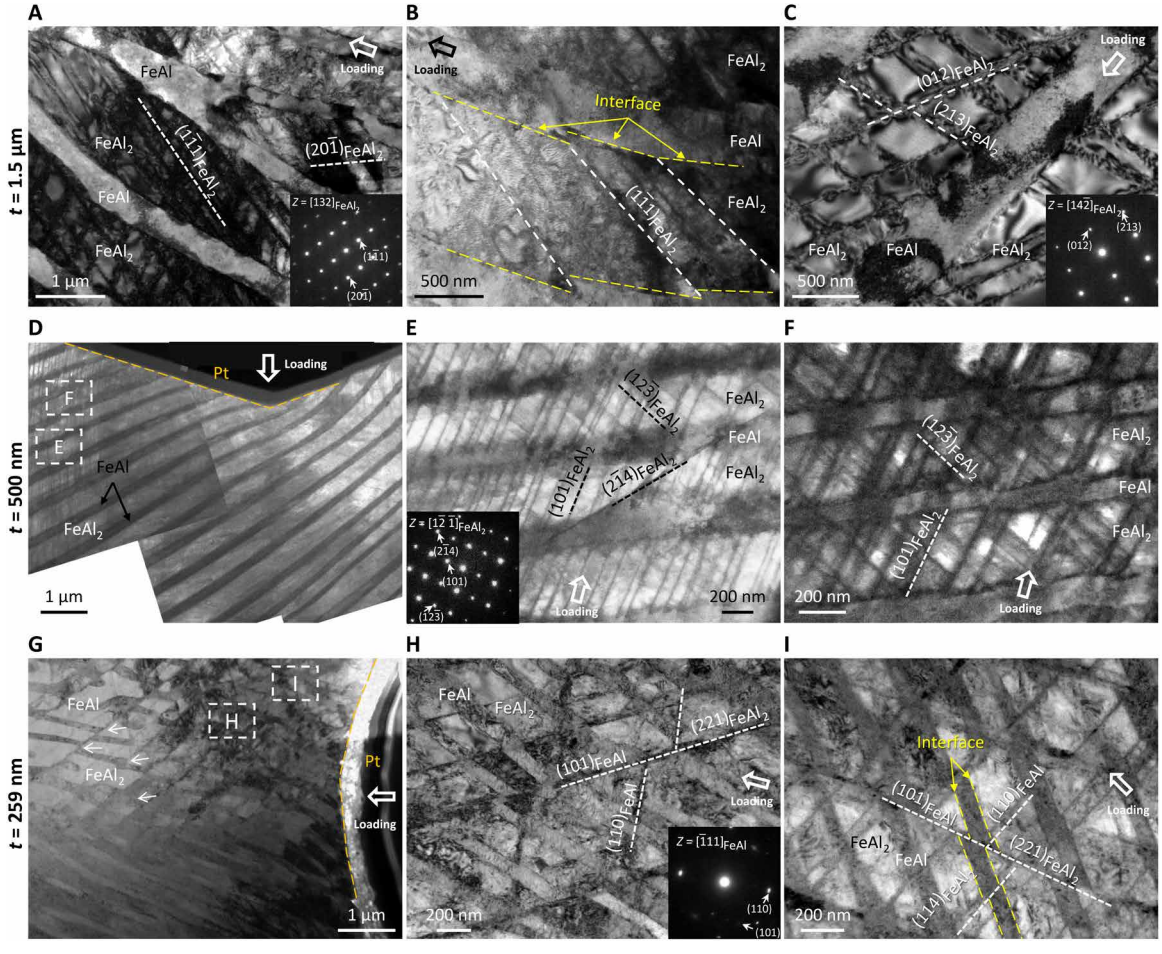

Fig. 4. Deformation of layered FeAl/$FeAl_2$ (t = 1.5 μm, 500 nm, and 259 nm). (**A** to **C**) TEM micrographs displaying the deformation microstructures underneath the indentation on a layered FeAl/$FeAl_2$ with an average layer thickness of 1.5 μm. (**D** to **F**) TEM micrographs of the microstructures formed beneath the indentation on a layered FeAl/$FeAl_2$ with an average layer thickness of 500 nm; slip localization and shear of the interface were identified. (**G** to **I**) TEM micrographs showing the deformation microstructures underneath the indentation on a layered FeAl/$FeAl_2$ with an average thickness of 259 nm. Slip bands have developed across many alternating FeAl/$FeAl_2$ layers.

with different orientations across layers, as shown in Fig. 4 (G to I). Figure 4G shows the corresponding indentation morphology. The layers have codeformed in plastic flow, permitting both phases to refine to even thinner thicknesses. No cracks can be identified around the indentation print. Figure 4G displays the dislocation substructures underneath the indenter. The FeAl and $FeAl_2$ layers still can be identified; however, these layers have been frequently sheared by two slip band variants, forming shear offsets, as indicated by the white arrows in Fig. 4G. Figure 4 (H and I) shows that the slip bands in the FeAl layers have developed mainly on the (110) and (101) planes, which are the major slip planes in the B2 FeAl phase. In the $FeAl_2$ layers, however, development of intense slip bands appears to have been suppressed. Observations of shear offsets at the interface and at the points of intersection of these two slip bands, as marked in Fig. 4I, suggest that the slip bands have frequently transmitted across the layers. Thus, enhanced slip transmission across the interface thwarted the slip bands from localizing and intensifying in the $FeAl_2$ layers. With the slip transmission induced in the finest layers, $FeAl_2$ codeformed with the ductile FeAl. This coplastic deformation between the FeAl and $FeAl_2$ layers is the key to realizing homogeneous plasticity and ductile-like failure behavior at room temperature in the normally brittle Fe-Al alloys.

Micropillar compression

To further test for the deformation ability of FeAl/$FeAl_2$ interfaces, micropillars were fabricated from a lamellar crystal in the material and tested in compression. Under nanoindentation of these pillars, the composite crystals deform by interfacial sliding, causing the individual layers to slide and protrude out into the free surface of the pillar. The micropillar compression test was repeated for different layer thicknesses (t = 1 μm to 500 nm) and compression-axis/layer orientation relationships, and in all cases, failure under the compressive load occurs by interfacial sliding. Figure 5 presents the deformed micropillars and the corresponding compressive stress-strain curves. The three micropillars display similar elastic to plastic transition behavior, but different levels of strain burst in the fully plastic region that follows. After compression, the morphologies of deformed pillars were examined by SEM. As demonstrated in Fig. 5 (B, D, and F), all plastic deformation takes place along the FeAl/$FeAl_2$ interfaces, as indicated by the slip offset formed on the surface of pillar. By measuring the angle between loading axis and the interface, the room-temperature critical resolved shear stress along the FeAl/$FeAl_2$ interface is estimated as 350 MPa. The easy glide of the FeAl/$FeAl_2$ interface provides another deformation path in the indentation deformation of the layered FeAl/$FeAl_2$ alloy, as demonstrated in fig. S3D. In the polycrystalline material, such runaway interfacial sliding would be constrained by the colony boundaries. The results here identify the $(11\bar{3})_{FeAl_2}//(101)_{FeAl}$ interface as a pseudo-slip system, which could act as an additional deformation mechanism that is more favorable than cracking.

DISCUSSION

Generalized stacking fault energy curves for the (101) ⟨111⟩ system in FeAl and $FeAl_2$

We performed density functional theory (DFT) calculations simulations to understand the energetics associated with shearing the {110} planes in these two materials. It is observed in TEM that while dislocations predominantly glide in {110} plane in FeAl, they only glide on this plane in $FeAl_2$ when the bilayer thickness t becomes sufficiently fine. Figure 6 shows computed generalized stacking fault energies (GSFE) curves associated with shear displacements in the {110}⟨111⟩ glide system in FeAl and $FeAl_2$. For both the FeAl and $FeAl_2$ phases, two cases are shown, one in which the simulation cell is driven to shear along the [111] direction but constrained to deform in the transverse direction (denoted as UR, unrelaxed), and the other when the constraint was lifted, allowing for it (denoted as R, relaxed) (*37*). Any differences in the energies are indicative of additional atomic shuffling (*38*, *39*). A local minimum in the GSFE is attained at a shear displacement a_0[111]/2 in FeAl. The relaxed curve, however, achieves a much lower potential energy overall, particularly at the local minimum, indicating that local atomic shuffling apart from the displacements along the slip direction is needed to accomplish the deformation. For $FeAl_2$, the same effect of relaxation is seen, also suggesting deformation by shear plus atomic shuffling. The reduction due to relaxation is more substantial in $FeAl_2$ than in FeAl. We can, therefore, expect that the shearing mechanism in this plane in $FeAl_2$ is much more complicated than the conventional picture of slip and would require relatively high stresses and aid of thermal energy for glide to be activated.

For FeAl, the {110}⟨111⟩ is the only system on which glide is seen experimentally for all layer thicknesses, and in simulation, the potential to shear this plane is five to six times lower than on $FeAl_2$. The substantially higher energies in the $FeAl_2$ phase suggest that deformation along the {110}⟨111⟩ glide system is unpreferred. This result is consistent with the finding that, apart from the 259-nm layered material, several other slip systems were used in the deformation of both single-phase $FeAl_2$ and the layered FeAl/$FeAl_2$ material.

It is likely that this very hard slip system is observed in TEM within the $FeAl_2$ crystals in the t = 259 nm case because the strong confinement imposed by the fine nanoscale dimensions on the dislocations hindered proliferating slip by gliding dislocations on multiple distinct planes. Under the nanoscale confinement, propagating slip becomes easier to achieve by transmitting slip across several adjacent crystals on the same slip system. The glide system of choice for slip transmission across the interface is the {110}⟨111⟩ system, the one shared by both crystals and, hence, provides a geometrically undisrupted slip pathway across the interface. The notion of nanoscale confinement suggests that there would exist a critical layer thickness below which slip transmission across the {110}⟨111⟩ system becomes favored and is determined by a subtle competition between multiple easy slip systems in the large crystal versus slip transmission involving a hard system in a nanocrystal. As we have seen here experimentally, attaining conditions for slip transmission leads to an unusual state of codeformation between the two phases and homogeneous, less catastrophic failure.

Synergy effects of the biphase interface on the BDT temperature of Fe-Al alloys

The FeAl/$FeAl_2$ interface plays a central role in mediating the BDT of Fe-Al alloy, as summarized in fig. S4, primarily by altering the failure behavior of the $FeAl_2$ layer. Alone, the $FeAl_2$ phase is brittle at room temperature and susceptible to strain localization followed by cracking (fig. S4A). By introducing FeAl/$FeAl_2$ interfaces, the $FeAl_2$ phase still maintains the tendency for strain localization and cracking, but they can be suppressed from propagating by the FeAl/$FeAl_2$ interfaces. Similar to other brittle/ductile layered materials systems, such as Al/TiN, plastic deformation starts in the ductile

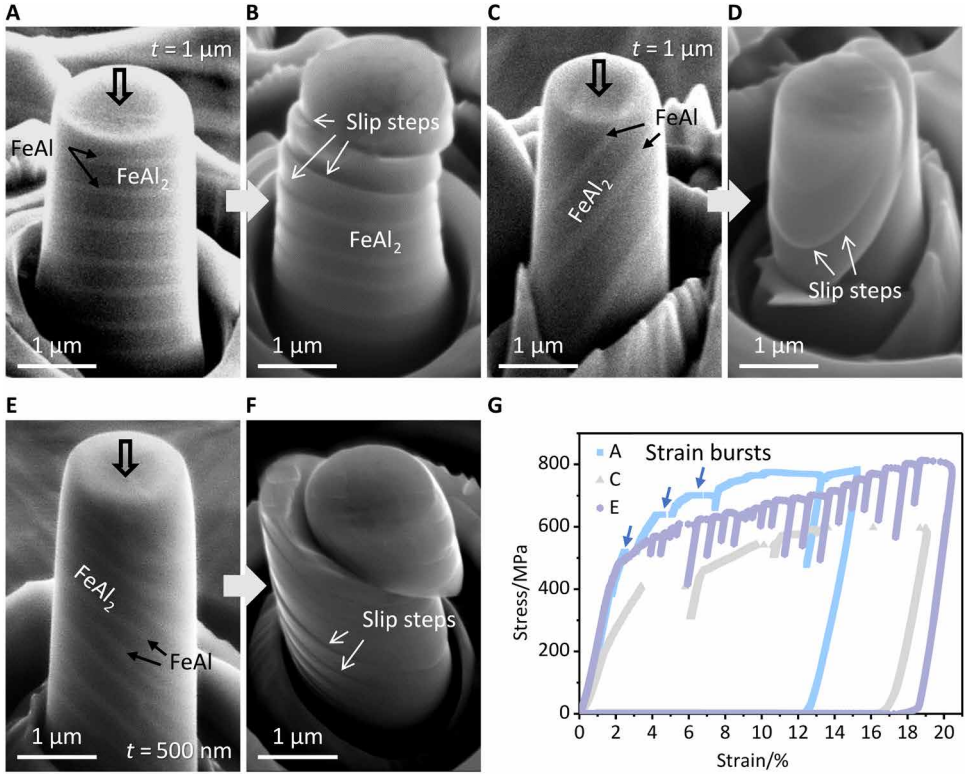

Fig. 5. Deformation of layered FeAl/$FeAl_2$ pillars. Typical SEM micrographs of the layered FeAl/$FeAl_2$ pillars before (**A**, **C**, and **E**) and after (**B**, **D**, and **F**) compression. The three pillars in (A), (C), and (E) have different layer orientations relative to the loading axis. (**G**) Typical compressive stress-strain curves of the layered FeAl/$FeAl_2$ pillars.

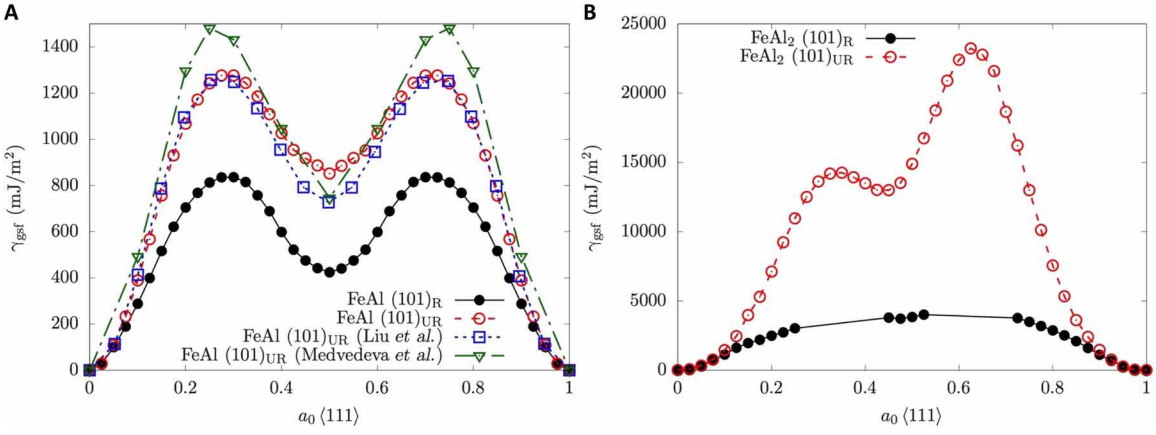

Fig. 6. GSFE curves of FeAl and $FeAl_2$. (**A**) Unrelaxed (UR) and relaxed (R) generalized stacking fault energies (GSFE) curves in the B2-ordered FeAl calculated here. Also shown for comparison are the (UR) results based on prior ab initio calculations from Liu *et al.* (*46*) and Medvedeva *et al.* (*47*). (**B**) UR and R GSFE curves in $FeAl_2$.

layers (*30*). As the moving dislocations in the ductile layers accumulate at the interface, their local stress fields will affect how deformation proceeds in the brittle one. This interface-enabled plasticity increases as the layer thickness decreases (*30*). With finer layer thicknesses, the FeAl/$FeAl_2$ interfaces can suppress cracking and occasionally block propagation of some of the intense slip bands formed in the $FeAl_2$ layer (fig. S4B). These mechanisms manifest by the formation of strain contrast at the interface in the FeAl layer (Fig. 3E), reducing the number of localized slip bands after passing the FeAl/$FeAl_2$ interface (Fig. 3F), producing short shear offsets along the FeAl/$FeAl_2$ interface (Fig. 4, B and E). When the layers' thicknesses reduce below 500 nm, plastic strain in the individual layers become delocalized, marked by weaker, more finely spaced slip bands. Another notable difference is the formation of two major variants of slip bands along the {110} crystallographic planes in both phases. Apparently, the interfaces force the brittle $FeAl_2$ layer to codeform with the ductile FeAl layers along the most close-packed crystallographic slip systems of FeAl (*30*). Apart from stopping and dispersing the localized strain from the bands, the FeAl/$FeAl_2$ interface can also serve as an easy pseudo-slip system, which can provide

a preferred deformation mechanism in addition to the slip inside layers.

In summary, we fabricate a layered eutectoid FeAl/$FeAl_2$ alloys with differing individual layer thicknesses from microns to nanometers and study their failure behavior at room temperature. A transition from brittle to ductile is realized in a eutectoid layered structure with sufficiently fine layer thicknesses below 1 μm. The nanoscale confinement enforced slip transmission on uncommon glide planes, enabling codeformation between an otherwise brittle $FeAl_2$ and already ductile FeAl layer. The consequence is a transition away from strain localization in the form of intense bands and crack formation and toward homogeneous deformation and ductile-like deformation at room temperature. These findings point to interface engineering and are valuable and promising methods for markedly reducing the BDT temperature of lightweight intermetallics.

METHODS

Experimental details

The eutectoid Fe-Al alloy with alternative FeAl/$FeAl_2$ layers was produced by arc melting of pure Al (99.99%) and Fe (99.99%) in a tube furnace. As marked in the phase diagram of Fe-Al binary alloy in Fig. 1A, the composition binary of this eutectoid alloy has an atomic ratio of Fe:Al = 39:61. An additional 2 weight % of Al is added before arc melting to avoid loss of Al during melting. After remelting several times, layered structures were produced. The thickness of the layers can be fine-tuned by the cooling rate, i.e., air cooling versus water quenching. The Fe-Al samples were cut into disks of dimensions 1 mm by Φ6 mm and polished following standard metallurgical procedures for microstructural observation and mechanical testing. Indentation and micropillar compression were carried out at room temperature. A load of 300 gf in the Micro Vickers hardness measurement is used for these tests. The nanoindentation and micropillar compression tests were performed using a Hysitron TI950 Triboindenter, while nanoindentation tests were performed using a Berkovich tip under a load of 5000 μN for 5 s. The micropillar tests used a flat tip for applying compression under the displacement control mode with a strain rate of 5×10^{-3} s^{-1}. The microstructures of Fe-Al alloy before and after deformation were characterized using a Hitachi SU6600 SEM equipped with energy-dispersive x-ray spectrometer systems. The defect microstructures after deformation were investigated using a JEOL 2100F TEM. Micropillars were prepared using a Helios NanoLab DualBeam FIB. Deformation microstructures underneath the indentation were observed by cutting thin foils on an indentation print made via the FIB sample-lifting technique.

DFT calculation

DFT calculations were conducted via Vienna Ab-initio Simulation Package (VASP) (*40*). In DFT, based on the projector augmented-wave method (*41*, *42*), a pseudo-potential using a plane-wave basis with a cutoff energy of 439.857 eV was adopted. To approximate the exchange-correlation energy functional, the Perdew-Burke-Ernzerhof formulation of the generalized gradient approximation was used (*43*). The conjugate gradient scheme was used for the electronic self-consistent loop. Convergence is reached when the total free-energy change between two sequential steps are smaller than 10^{-4} eV. The Brillouin zone was constructed by the Monkhorst-Pack scheme (*44*), with a smearing width of 0.2 eV based on the Methfessel-Paxton smearing method (*45*). Spin-polarization is considered only for the Fe atoms, which are ferromagnetic.

SUPPLEMENTARY MATERIALS

Supplementary material for this article is available at http://advances.sciencemag.org/cgi/content/full/6/39/eabb6658/DC1

REFERENCES AND NOTES

1. Z. Liu, G. Wei, F. Wang, Oxidation behaviour of FeAl intermetallic coatings produced by magnetron sputter deposition. *Scr. Mater.* **39**, 1497–1502 (1998).
2. N. S. Stoloff, Iron aluminides: Present status and future prospects. *Mater. Sci. Eng. A* **258**, 1–14 (1998).
3. C. T. Liu, E. P. George, P. J. Maziasz, J. H. Schneibel, Recent advances in B2 iron aluminide alloys: Deformation, fracture and alloy design. *Mater. Sci. Eng. A* **258**, 84–98 (1998).
4. J. Cebulski, D. Pasek, *FeAl Intermetallic Alloy: Its Heat-resistant and Practical Application, Intermetallic Compounds -Formation and Applications*, M. Aliofkhazraei, Ed., Books on Demand (2018).
5. D. G. Morris, M. A. Muñoz-Morris, Recent developments toward the application of iron aluminides in fossil fuel technologies. *Adv. Eng. Mater.* **13**, 43–47 (2011).
6. G. Zhang, X. Wang, F. Yang, Y. Shi, J. Song, X. Lai, Energetics and diffusion of hydrogen in hydrogen permeation barrier of α-Al_2O_3/FeAl with two different interfaces. *Int. J. Hydrogen Energy* **38**, 7550–7560 (2013).
7. C. T. Liu, J. Stringer, J. N. Mundy, L. L. Horton, P. Angelini, Ordered intermetallic alloys: An assessment. *Intermetallics* **5**, 579–596 (1997).
8. C.-H. Zhang, S. Huang, S. Jiang, N.-X. Chen, Structural and mechanical properties of Fe–Al compounds: An atomistic study by EAM simulation. *Intermetallics* **52**, 86–91 (2014).
9. P. Matysik, S. Jóźwiak, T. Czujko, Characterization of low-symmetry structures from phase equilibrium of Fe-Al system—Microstructures and mechanical properties. *Mateials.* **8**, 914–931 (2015).
10. O. Ikeda, I. Ohnuma, R. Kainuma, K. Ishida, Phase equilibria and stability of ordered BCC phases in the Fe-rich portion of the Fe-Al system. *Intermetallics* **9**, 755–761 (2001).
11. I. B. Baker, P. R. Munroe, Mechanical properties of FeAl. *Int. Mater. Rev.* **42**, 181–205 (1997).
12. D. Risanti, J. Deges, L. Falat, S. Kobayashi, J. Konrad, M. Palm, B. Pöter, A. Schneider, C. Stallybrass, F. Stein, Dependence of the brittle-to-ductile transition temperature (BDTT) on the Al content of Fe–Al alloys. *Intermetallics* **13**, 1337–1342 (2005).
13. M. G. Mendiratta, H.-M. Kim, H. A. Lipsitt, Slip directions in B2 Fe-Al alloys. *Metall. Trans. A* **15**, 395–399 (1984).
14. X. Li, A. Schmitt, M. Heilmaier, F. Stein, The Al-rich part of the Fe-Al phase diagram. *J. Phase Equilib. Diffus.* **37**, 162–163 (2016).
15. X. Li, A. Schmitt, M. Heilmaier, F. Stein, The effect of the ternary elements B, Ti, Cr, Cu, and Mo on fully lamellar FeAl + $FeAl_2$ alloys. *J. Alloy. Compd.* **722**, 219–228 (2017).
16. H. Clemens, S. Mayer, Design, processing, microstructure, properties, and applications of advanced intermetallic TiAl alloys. *Adv. Eng. Mater.* **15**, 191–215 (2013).
17. A. Misra, J. P. Hirth, R. G. Hoagland, Length-scale-dependent deformation mechanisms in incoherent metallic multilayered composites. *Acta Mater.* **53**, 4817–4824 (2005).
18. J. Wang, R. G. Hoagland, J. P. Hirth, A. Misra, Atomistic modeling of the interaction of glide dislocations with "weak" interfaces. *Acta Mater.* **56**, 5685–5693 (2008).
19. D. Yu, H. Bei, Y. Chen, E. P. George, K. An, Phase-specific deformation behavior of a relatively tough NiAl–Cr(Mo) lamellar composite. *Scr. Mater.* **84-85**, 59–62 (2014).
20. S. J. Wang, G. Liu, D. Y. Xie, Q. Lei, B. P. Ramakrishnan, J. Mazumder, J. Wang, A. Misra, Plasticity of laser-processed nanoscale Al-Al_2Cu eutectic alloy. *Acta Mater.* **156**, 52–63 (2018).
21. J.-W. Zhang, I. J. Beyerlein, W.-Z. Han, Hierarchical 3D nanolayered duplex-phase Zr with high strength, strain hardening and ductility. *Phys. Rev. Lett.* **122**, 255501 (2019).
22. W. Z. Han, M. J. Demkowicz, E. G. Fu, Y. Q. Wang, A. Misra, Effect of grain boundary character on sink efficiency. *Acta Mater.* **60**, 6341–6351 (2012).
23. W.-Z. Han, M. J. Demkowicz, N. A. Mara, E. G. Fu, S. Sinha, A. D. Rollett, Y. Wang, J. S. Carpenter, I. J. Beyerlein, A. Misra, Design of radiation tolerant materials via interface engineering. *Adv. Mater.* **25**, 6975–6979 (2013).
24. I. J. Beyerlein, A. Caro, M. J. Demkowicz, N. A. Mara, A. Misra, B. P. Uberuaga, Radiation damage tolerant nanomaterials. *Mater. Today* **16**, 443–449 (2013).
25. E. G. Fu, A. Misra, H. Wang, L. Shao, X. Zhang, Interface enabled defects reduction in helium ion irradiated Cu/V nanolayers. *J. Nucl. Mater.* **407**, 178–188 (2010).
26. M. Wang, I. J. Beyerlein, J. Zhang, W.-Z. Han, Defect-interface interactions in irradiated Cu/Ag nanocomposites. *Acta Mater.* **160**, 211–223 (2018).
27. M. Wang, I. J. Beyerlein, J. Zhang, W.-Z. Han, Bi-metal interface-mediated defects distribution in neon ion bombarded Cu/Ag nanocomposites. *Scr. Mater.* **171**, 1–5 (2019).

28. A. Donohue, F. Spaepen, R. G. Hoagland, A. Misra, Suppression of the shear band instability during plastic flow of nanometer-scale confined metallic glasses. *Appl. Phys. Lett.* **91**, 241905 (2007).
29. J. Wang, A. Misra, Strain hardening in nanolayered thin films. *Curr. Opin. Solid State Mater. Sci.* **18**, 19–28 (2014).
30. N. Li, H. Wang, A. Misra, J. Wang, In situ nanoindentation study of plastic co-deformation in Al-TiN nanocomposites. *Sci. Rep.* **4**, 6633 (2015).
31. A. Schmitt, K. S. Kumar, A. Kauffmann, M. Heilmaier, Microstructural evolution during creep of lamellar eutectoid and off-eutectoid FeAl/$FeAl_2$ alloys. *Intermetallics* **107**, 116–125 (2019).
32. H. Wang, T. Harrington, C. Y. Zhu, K. S. Vecchio, Design, fabrication and characterization of FeAl-based metallic-intermetallic laminate (MIL) composites. *Acta Mater.* **175**, 445–456 (2019).
33. F. Stein, S. C. Vogel, M. Eumann, M. Palm, Determination of the crystal structure of the ε phase in the Fe–Al system by high-temperature neutron diffraction. *Intermetallics* **18**, 150–156 (2010).
34. I. Chumak, K. W. Richter, H. Ehrenberg, Redetermination of iron dialuminide, $FeAl_2$. *Acta Crystallogr.* **66**, i87–i88 (2010).
35. A. Scherf, A. Kauffmann, S. Kauffmann-Weiss, T. Scherer, X. Li, F. Stein, M. Heilmaier, Orientation relationship of eutectoid FeAl and $FeAl_2$. *J. Appl. Crystallogr.* **49**, 442–449 (2016).
36. A. Misra, J. P. Hirth, R. G. Hoagland, J. D. Embury, H. Kung, Dislocation mechanisms and symmetric slip in rolled nano-scale metallic multilayers. *Acta Mater.* **52**, 2387–2394 (2004).
37. Y. Su, S. Xu, I. J. Beyerlein, Density functional theory calculations of generalized stacking fault energy surfaces for eight face-centered cubic transition metals. *J. Appl. Phys.* **126**, 105112 (2019).
38. A. Kumar, M. Arul Kumar, I. J. Beyerlein, First-principles study of crystallographic slip modes in ω-Zr. *Sci. Rep.* **7**, 8932 (2017).
39. A. Kumar, B. M. Morrow, R. J. McCabe, I. J. Beyerlein, An atomic-scale modeling and experimental study of $\langle c + a \rangle$ dislocations in Mg. *Mater. Sci. Eng. A* **695**, 270–278 (2017).
40. G. Kresse, J. Furthmüller, Efficient iterative schemes for ab initio total-energy calculations using a plane-wave basis set. *Phys. Rev. B* **54**, 11169 (1996).
41. P. E. Blöchl, Projector augmented-wave method. *Phys. Rev. B* **50**, 17953 (1994).
42. G. Kresse, D. Joubert, From ultrasoft pseudopotentials to the projector augmented-wave method. *Phys. Rev. B* **59**, 1758 (1999).
43. J. P. Perdew, K. Burke, M. Ernzerhof, Generalized gradient approximation made simple. *Phys. Rev. Lett.* **77**, 3865–3868 (1996).
44. H. J. Monkhorst, J. D. Pack, Special points for Brillouin-zone integrations. *Phys. Rev. B* **13**, 5188 (1976).
45. M. Methfessel, A. T. Paxton, High-precision sampling for Brillouin-zone integration in metals. *Phys. Rev. B* **40**, 3616 (1989).
46. L. Liu, X. Wu, R. Wang, W. Li, Q. Liu, First principle study on the temperature dependent elastic constants, anisotropy, generalized stacking fault energy and dislocation core of NiAl and FeAl. *Comput. Mater. Sci.* **103**, 116–125 (2015).
47. N. I. Medvedeva, O. N. Mryasov, Y. N. Gornostyrev, D. L. Novikov, A. J. Freeman, First-principles total-energy calculations for planar shear and cleavage decohesion processes in *B2*-ordered NiAl and FeAl. *Phys. Rev. B* **54**, 13506 (1996).

Acknowledgments

Funding: This research was supported by the National Key Research and Development Program of China (2017YFB0702301), the National Natural Science Foundation of China (grant nos. 51971170, 51922082, and 51942104), the 111 Project of China (grant number BP2018008), and the Innovation Project of Shaanxi Province (grant no. 2017KTPT-12). **Author contributions:** W.-Z.H. and I.J.B. designed the project. L.-L.L. performed the experiments under the guidance of W.-Z.H. Y.Q.S. and I.J.B. conducted simulations. L.-L.L., I.J.B., and W.-Z.H wrote the manuscript. All the authors discussed and analyzed the data and given approval to the final version of the manuscript. **Competing interests:** The authors declare that they have no competing interests. **Data and materials availability:** All data needed to evaluate the conclusions in the paper are present in the paper and/or the Supplementary Materials. Additional data related to this paper may be requested from the authors.

Submitted 10 March 2020
Accepted 7 August 2020
Published 23 September 2020
10.1126/sciadv.abb6658

Citation: L.-L. Li, Y. Q. Su, I. J. Beyerlein, W.-Z. Han, Achieving room-temperature brittle-to-ductile transition in ultrafine layered Fe-Al alloys. *Sci. Adv.* **6**, eabb6658 (2020).

Achieving room-temperature brittle-to-ductile transition in ultrafine layered Fe-Al alloys

Lu-Lu Li, Yanqing Su, Irene J. Beyerlein and Wei-Zhong Han

Sci Adv **6** (39), eabb6658.
DOI: 10.1126/sciadv.abb6658